

Phonon promoted charge density wave in topological kagome metal ScV₆Sn₆

Yong Hu^{1,#,*}, Junzhang Ma^{2,3,4,#}, Yinxiang Li^{5,#}, Dariusz Jakub Gawryluk⁶, Tianchen Hu⁷, Jérémie Teyssier⁸, Volodymyr Multian⁸, Zhouyi Yin⁹, Yuxiao Jiang¹⁰, Shuxiang Xu⁷, Soohyeon Shin⁶, Igor Plokhikh⁶, Xinloong Han¹¹, Nicholas Clark Plumb¹, Yang Liu¹², Jiaxin Yin¹³, Zurab Guguchia¹⁴, Yue Zhao⁹, Andreas P. Schnyder¹⁵, Xianxin Wu^{16,*}, Ekaterina Pomjakushina⁶, M. Zahid Hasan¹⁰, Nanlin Wang^{7,17,18}, and Ming Shi^{1,12,*}

¹Photon Science Division, Paul Scherrer Institut, CH-5232 Villigen PSI, Switzerland

²Department of Physics, City University of Hong Kong, Kowloon, Hong Kong, China

³City University of Hong Kong Shenzhen Research Institute, Shenzhen, China

⁴Hong Kong Institute for Advanced Study, City University of Hong Kong, Kowloon, Hong Kong, China

⁵College of Science, University of Shanghai for Science and Technology, Shanghai, 200093, China

⁶Laboratory for Multiscale Materials Experiments, Paul Scherrer Institut, CH-5232 Villigen PSI, Switzerland

⁷International Center for Quantum Materials, School of Physics, Peking University, Beijing 100871, China

⁸Department of Quantum Matter Physics, University of Geneva, 24 Quai Ernest-Ansermet, 1211 Geneva 4, Switzerland

⁹Institute for Quantum Science and Engineering and Department of Physics, Southern University of Science and Technology of China, Shenzhen, Guangdong 518055, China

¹⁰Laboratory for Topological Quantum Matter and Advanced Spectroscopy (B7), Department of Physics, Princeton University, Princeton, NJ, USA

¹¹Kavli Institute for Theoretical Sciences, University of Chinese Academy of Sciences, Beijing 100190, China

¹²Center for Correlated Matter and Department of Physics, Zhejiang University, Hangzhou 310058, China

¹³Department of physics, Southern University of Science and Technology, Shenzhen, Guangdong 518055, China

¹⁴Laboratory for Muon Spin Spectroscopy, Paul Scherrer Institute, CH-5232 Villigen PSI, Switzerland

¹⁵Max-Planck-Institut für Festkörperforschung, Heisenbergstrasse 1, D-70569 Stuttgart, Germany

¹⁶CAS Key Laboratory of Theoretical Physics, Institute of Theoretical Physics, Chinese Academy of Sciences, Beijing 100190, China

¹⁷Beijing Academy of Quantum Information Sciences, Beijing 100913, China

¹⁸Collaborative Innovation Center of Quantum Matter, Beijing 100871, China

#These authors contributed equally to this work.

*To whom correspondence should be addressed:

Y.H. (yonghphysics@gmail.com); X.W. (xxwu@itp.ac.cn); M.S. (ming.shi@psi.ch)

Charge density wave (CDW) orders in vanadium-based kagome metals have recently received tremendous attention due to their unique properties and intricate interplay with exotic correlated phenomena, topological and symmetry-breaking states. However, the origin of the CDW order remains a topic of debate. The discovery of ScV₆Sn₆, a vanadium-based bilayer kagome metal exhibiting an in-plane $\sqrt{3} \times \sqrt{3}$ R30° CDW order with time-reversal symmetry breaking, provides a novel platform to explore the underlying mechanism behind the unconventional CDW. Here, we combine high-resolution angle-resolved photoemission spectroscopy, Raman scattering measurements and density functional theory to investigate the electronic structures and phonon modes of ScV₆Sn₆ and their evolution with temperature. We identify topologically nontrivial Dirac

surface states and multiple van Hove singularities (VHSs) in the vicinity of the Fermi level, with one VHS near the \bar{K} point exhibiting nesting wave vectors in proximity to the $\sqrt{3} \times \sqrt{3}$ $R30^\circ$ CDW wave vector. Additionally, Raman measurements indicate a strong intrinsic electron-phonon coupling in ScV_6Sn_6 , as evidenced by the presence of a two-phonon mode and a large frequency amplitude mode. Our findings highlight the fundamental role of lattice degrees of freedom in promoting the CDW in ScV_6Sn_6 and provide important insights into the fascinating correlation phenomena observed in kagome metals.

The kagome lattice, a corner-sharing triangle network, has emerged as a versatile platform for exploring unconventional correlated and topological quantum states. Due to the unique correlation effects and frustrated lattice geometry inherent to kagome lattices, several families of kagome metals have been found to display a variety of unconventional electronic instabilities and nontrivial topologies, including quantum spin liquid [1-3], unconventional superconductivity [4-7], charge density wave (CDW) orders [5-7], and Dirac/Weyl semimetals [8-10]. Of particular interest are the recently discovered non-magnetic vanadium-based superconductors AV_3Sb_5 ($A=\text{K, Rb, Cs}$), which exhibit intriguing similarities to correlated electronic phenomena observed in high-temperature superconductors, such as CDW [11-13], pair density wave [14], and electronic nematicity [15]. Especially, the three-dimensional (3D) CDW order with an in-plane 2×2 reconstruction possesses exotic properties, including time-reversal symmetry breaking [12,16,17], intertwined with unconventional superconductivity [17], and rotational symmetry breaking [13,14]. Two possible scenarios, namely phonon softening [18,19] and correlation-driven Fermi surface (FS) instability [20-23], have been proposed to account for the CDW order. However, despite intense research efforts, the origin of the CDW order and its symmetry-breaking characteristics remain elusive.

Very recently, a new family of vanadium-based bilayer kagome metals, RV_6Sn_6 (where R represents a rare-earth element), has been discovered [24,25]. Although its kagome layer does not show long-range magnetic order, similar to AV_3Sb_5 , magnetism can be introduced by controlling the R sites, providing a tunable platform to investigate magnetism, nontrivial topology and correlation effects native to the kagome lattice. Notably, ScV_6Sn_6 , a member of the bilayer kagome family, undergoes an intriguing 3D CDW phase transition with a wave-vector $\mathbf{Q} = (1/3, 1/3, 1/3)$ below $T_{\text{CDW}} \sim 92 \text{ K}$ [26], unlike the CDW observed in AV_3Sb_5 . Interestingly, recent experimental evidence shows that time-reversal symmetry breaking also occurs in the CDW state [27]. However, the nature of the CDW and its driving force remain unresolved. An in-depth investigation of the band structure and its interplay with lattice vibrations in ScV_6Sn_6 would provide valuable insights into the mechanism underlying the CDW order with intriguing symmetry-breaking in kagome metals.

Here, we investigate the electronic and lattice degrees of freedom in the CDW formation of the kagome metal ScV_6Sn_6 using a combination of scanning tunneling microscopy (STM), high-resolution angle-resolved photoemission spectroscopy (ARPES), Raman scattering measurements and density functional theory (DFT). Our low-temperature STM topographs visualize an in-plane $\sqrt{3} \times \sqrt{3}$ $R30^\circ$

reconstruction, corresponding to the bulk CDW wavevector measured in diffraction experiments [26]. In the electronic structure, we identify topologically nontrivial Dirac surface states (TDSSs) and multiple van Hove singularities (VHSs) in the vicinity of the Fermi level (E_F). Intriguingly, the nesting vector connecting the VHSs near the \bar{K} point is close to $(1/3, 1/3)$, matching with the observed $\sqrt{3} \times \sqrt{3}$ $R30^\circ$ CDW wave vector. In contrast to AV_3Sb_5 , however, pronounced band reconstructions appear to be absent in the CDW state of ScV_6Sn_6 , possibly due to the 3D nature of the $\sqrt{3} \times \sqrt{3} \times 3$ CDW order and a noticeable dispersion along the c -direction. Remarkably, our Raman measurements reveal the presence of a two-phonon mode in the normal state and Raman-active amplitude modes in the CDW phase, indicating a strong electron-phonon coupling. Collectively, our results emphasize the crucial role of lattice degrees of freedom in promoting the CDW in ScV_6Sn_6 and contribute to a deeper understanding of the diverse quantum correlation phenomena observed in vanadium-based kagome metals.

The pristine phase of ScV_6Sn_6 crystallizes in a layered structure with the space group $P6/mmm$. The unit cell consists of two V_3Sn^1 kagome layers, with Sn^2 and $ScSn^3_2$ layers stacked in an alternating fashion along the out-of-plane direction (c -axis) (Fig. 1a). Similar to the sister compound GdV_6Sn_6 , ScV_6Sn_6 tends to cleave along the c -axis, resulting in three surface terminations, namely the kagome, $ScSn^3_2$ and Sn^2 layers [28,29]. The electrical resistivity [Fig. 1b(i)] and specific heat capacity [Fig. 1b(ii)] measurements consistently show a transition around 92 K, indicating the presence of the CDW transition [26,30]. To study the superlattice modulation of the CDW, we perform comparative STM measurements on ScV_6Sn_6 in both the normal state (Fig. 1c) and the CDW phase (Fig. 1d). Atomically resolved STM topographies clearly identify the hexagonal lattice formed by the Sn^2 atoms [Figs. 1c(i) and 1d(i)] and the in-plane modulation in the CDW phase [inset of Fig. 1d(i)]. The Fourier transform of the topographic data further visualizes the existence of a $\sqrt{3} \times \sqrt{3}$ $R30^\circ$ reconstruction in the CDW phase [Fig. 1d(ii)], which is absent in the normal state [Fig. 1c(ii)]. Figure 1e displays the bulk Brillouin zone (BZ) and the projected two-dimensional (2D) surface BZ. In the CDW phase, the in-plane component of the CDW folds the pristine BZ [Fig. 1f(i)] into the new smaller $\sqrt{3} \times \sqrt{3}$ BZ [Fig. 1f(ii)].

We next focus on the electronic structure of the bilayer kagome metal ScV_6Sn_6 (Fig. 2). Utilizing high-resolution ARPES measurements with a small beam spot, we reveal three different sets of ARPES spectra associated with the three possible surface terminations on the cleaved sample surface (Figs. 2a, 2g, and Fig. S1). As previously established in GdV_6Sn_6 compound [29], the surface terminations of the sample can be identified by measuring the Sn 4d core level (Figs. 2b and 2h). In Figs. 2b-2f and Figs. 2h-2l, we present the electronic structure from the kagome (Fig. 2a) and $ScSn^3_2$ terminations (Fig. 2g), respectively. The measured FS, with pristine BZ (the dashed red lines in Figs. 2c and 2i) and high-symmetry points ($\bar{\Gamma}$, \bar{K} and \bar{M}) labeled, features a characteristic hexagonal kagome Fermiology, as generally exhibited in other kagome systems [8,10,11,29,31]. To visualize the energy-momentum dispersion of the electronics structures, polarization-dependent measurements were performed along two different high-symmetry paths, $\bar{\Gamma} - \bar{M}$ (Figs. 2d and 2j) and $\bar{\Gamma} - \bar{K}$ (Figs. 2e and 2k) directions.

Similar to other vanadium-based kagome metals [31,32], the photoemission intensities are strongly sensitive to the photon polarization (Figs. 2d-2e and 2j-2k), reflecting the multi-orbital nature of *V-d* orbitals. In contrast to AV_3Sb_5 , the photon-energy dependent measurements along the $\bar{\Gamma} - \bar{K}$ direction (Figs. 2f and 2l) exhibits distinct band dispersions at different k_z planes (also see Fig. S2), indicating the relatively obvious three-dimensionality of the electronic structure in ScV_6Sn_6 .

A comparative examination of the band structure on different terminations reveals some differences, which can be attributed to the presence of surface states and matrix element effects. Specifically, on the $ScSn^3_2$ termination, the measured FS centered around the $\bar{\Gamma}$ point consists of a circular-shaped and a hexagonal-shaped FS sheet, as illustrated in Fig. 3a. A closer inspection of the band dispersion, as depicted in Fig. 3b, indicates that these FS sheets around $\bar{\Gamma}$ arise from two V-shaped bands, which bear a striking resemblance to the TDSSs previously observed in GdV_6Sn_6 [29]. Our DFT calculations (see Fig. S3 for details) confirm these observations and highlight that the observed V-shaped bands around the $\bar{\Gamma}$ point (Fig. 3b) are indicative of the existence of TDSSs originating from a \mathbb{Z}_2 bulk topology in ScV_6Sn_6 .

Furthermore, in addition to the TDSSs, the ARPES spectra collected on the $ScSn^3_2$ termination reveal more details of the kagome bands, such as the characteristic Dirac cone (DC) and VHSs expected from the kagome tight-binding model [5,6]. Constant energy maps shown in Fig. 3c reveal two Dirac cones around the \bar{K} point. The energy–momentum dispersion along the $\bar{\Gamma} - \bar{K} - \bar{M} - \bar{\Gamma}$ direction (Fig. 3d), which agrees well with the calculated bulk states projected onto the (001) surface (Fig. 3e), confirms the existence of Dirac cones at binding energies (E_B) of 0.09 eV (DC1) and 0.28 eV (DC2), despite some differences in the energies of Dirac points between experimental data and theoretical calculations. Additionally, the band forming the DC2 extends to the \bar{M} point and constitutes a VHS (labeled as VHS1 in Figs. 3d and 3e). The saddle point nature of VHS1 is evident from cuts taken vertically across the $\bar{K} - \bar{M}$ path (#M₁-#M₅, as indicated in Fig. 3f), where the band bottom of the electron-like band (dashed green curve in Fig. 3g) exhibits a maximum energy slightly above E_F at the \bar{M} point (green solid curve). Furthermore, another hole-like band observed in Fig. 3h (same as Fig. 3g), which is slightly below the VHS1 band, has a minimum energy at the \bar{M} point, indicating the electron-like nature along the orthogonal direction (the blue curve in Fig. 3h). This feature demonstrates another van Hove band with the opposite dispersion close to E_F (marked as VHS2 in Figs. 3d). These twofold concavity VHSs are consistent with theoretical calculations (Fig. 3e) and have been identified in AV_3Sb_5 [31,33], where they are believed to promote the CDW order. Interestingly, we also identify an unusual VHS (referred to as VHS3) contributed by the DC1 band near the \bar{K} point, as highlighted by the dashed red curve in Fig. 3d. To further confirm the saddle point nature of VHS3, we examine the band dispersions perpendicular to the $\bar{\Gamma} - \bar{K}$ direction (cuts #K₁-#K₅ in Figs. 3f and 3i). The series of cuts in Fig. 3i reveal a hole-like band (dashed red curve) with a band bottom that exhibits a minimum energy at the $\bar{\Gamma}$ point. These are fully consistent with our calculations shown in the inset

of Fig. 3e, confirming its van Hove nature (see also Fig. S4). Due to the six-fold rotational symmetry of the lattice, there are six such saddle points near \bar{K} and \bar{A} , as shown in Fig. 3j(ii).

As VHSs carry large density of states and can promote competing electronic instabilities, we now explore the potential contribution of the identified multiple VHSs to the CDW in ScV_6Sn_6 . Previous theoretical studies have emphasized that VHSs located at the M point can naturally give rise to nesting vectors $Q_{1,2,3}$ [5,6] that connect different sublattices on the saddle points of the FS [Fig. 4a(i)], potentially leading to a 2×2 bond CDW instability. However, we note that the suggested FS nesting wave vectors $Q_{1,2,3}$ in Fig. 3j(i) are incompatible with the in-plane $\sqrt{3} \times \sqrt{3}$ $R30^\circ$ reconstruction observed in ScV_6Sn_6 [Fig. 1d(ii)]. Nevertheless, the nesting vectors associated with the identified VHS3 near the \bar{K} point are in proximity to $(1/3, 1/3)$ [Fig. 3j(ii)], which is more consistent with the observed in-plane $\sqrt{3} \times \sqrt{3}$ CDW pattern. To assess the role of VHS3 in the CDW formation, we perform temperature-dependent measurements on the band dispersions along the $\bar{\Gamma} - \bar{K}$ direction. Surprisingly, our high-resolution ARPES spectra show negligible differences between the CDW phase and normal state (Figs. 3k and 3l), in contrast to the significant band reconstructions observed in AV_3Sb_5 [32,34]. As the $V-3d$ states dominate near the E_F , this weak band reconstruction and folding effect may be due to the 3D nature of the $\sqrt{3} \times \sqrt{3} \times 3$ CDW order, where the distortion of V atoms is small [26], and noticeable dispersion along the c -direction (Fig. S2).

After investigating the electronic structure of ScV_6Sn_6 , we next examine the effects of the lattice degrees of freedom on the CDW formation using Raman scattering. Figure 4a displays a colormap of the Raman response, covering a temperature from 24 K to 200 K. The Raman spectra (Figs. 4a and 4b) feature two prominent Raman-active phonon peaks at 143 cm^{-1} and 243 cm^{-1} , which we attribute to the E_{2g} and A_{1g} modes, respectively, based on the polarization-dependent measurements (for details see Fig. S5) and theoretical calculations (Fig. 4c). Additionally, we observe multiple weak peak-like structures below 100 cm^{-1} (Fig. S5) and a broad peak around 116 cm^{-1} (highlighted by the dashed white curve in Fig. 4a and red arrow in Fig. 4b) in the spectra above T_{CDW} (indicated by the dashed red line in Fig. 4a). The weak peaks below 100 cm^{-1} , showing almost no temperature dependence (Fig. S5), likely arise from rotational spectrum of O_2 and N_2 along the laser path [35]. As the temperature decreases, both the E_{2g} and A_{1g} modes exhibit a blueshift (Fig. S5), while the broad peak around 116 cm^{-1} shifts minimally above T_{CDW} , but abruptly vanishes below T_{CDW} (Fig. 4b). The temperature-dependent behavior of the broad peak resembles the one observed in other well-studied CDW materials [36-39], indicating the presence of a two-phonon Raman mode. This mode involves two phonons with opposite wave vectors and represents a second order process usually correlated with the strong momentum dependent electron-phonon coupling near the CDW wave vector [37,40-42]. In ScV_6Sn_6 , the observed two-phonon mode likely originates from the acoustic longitudinal modes in the K - H path [Fig. 4f(ii), the shaded region highlights the half frequency of the two-phonon mode], according to the theoretical phonon dispersion in Fig. 4f. Below T_{CDW} , the two-phonon mode disappears, possibly due to CDW-induced phonon folding and alteration of electron-phonon coupling.

Moreover, multiple new phonon peaks (labeled as A_1 - A_4 in Fig. 4b) emerge below T_{CDW} , around 150 cm^{-1} and 240 cm^{-1} , indicating their intimate relationship with the CDW order. Interestingly, the two new modes (A_1 , A_2) close to the E_{2g} have almost no specific temperature dependence in their frequencies and linewidths (Figs. 4a and 4b) as the temperature approaches T_{CDW} , consistent with characteristics of CDW zone-folded modes. In contrast, the A_3 mode shows noticeable softening and broadening with warming towards T_{CDW} (Figs. 4d and 4e), eventually becoming unresolvable above T_{CDW} (Figs. 4a, 4b, 4d and 4e). These are indicative of a CDW amplitude mode derived from the collapse of coherent CDW order near T_{CDW} [36-39,43].

Our theoretical calculations show that imaginary phonon modes appear at the H and L points (Fig. 4f), corresponding to $\sqrt{3} \times \sqrt{3} \times 2$ and $2 \times 2 \times 2$ lattice reconstructions, respectively. However, these modes, along with the absence of unstable phonon modes at $(1/3, 1/3, 1/3)$ (Fig. 4f), fail to explain the observed $\sqrt{3} \times \sqrt{3} \times 3$ CDW order. This suggests that the bare phonon instability is insufficient to account for the CDW order in our experiments (Figs. 1b and 1d). Our identification of the two-phonon mode order, typically much weaker than the one-phonon Raman modes, points to a strong electron-phonon coupling in ScV_6Sn_6 . This coupling could induce significant phonon softening at the CDW vector by introducing a negative self-energy term through the electron bubble. Consequently, the renormalized phonon dispersion may exhibit an anomaly and a minimum negative frequency at the wave vector $\mathbf{Q} = (1/3, 1/3, 1/3)$, giving rise to the observed CDW order. Our Raman measurements support this scenario, as they show the absence of one-phonon softening modes and the observation of amplitude modes with high frequency [44]. Furthermore, the nesting vector between the observed VHSs around the \bar{K} point [Fig. 3j(ii)] aligns with the in-plane component of the CDW vector, suggesting that electronic correlation may also participate in promoting the in-plane component of CDW order [45].

Finally, we discuss the possible origin of time-reversal symmetry breaking charge order in the non-magnetic vanadium-based kagome metals AV_3Sb_5 [12,16,17] and ScV_6Sn_6 [27]. While the CDW order in both systems shares some similarities, there are two main differences. First, in AV_3Sb_5 , the CDW pattern mainly results from the distortion of the kagome V atoms (Fig. 4g) [32,46,47]. In contrast, in ScV_6Sn_6 , the CDW order mainly involves the displacement of Sc and Sn, while the V atoms show negligible distortion (Fig. 4h) [26]. Second, the presence of a two-phonon mode and a large frequency amplitude mode in ScV_6Sn_6 suggests a much stronger electron-phonon coupling than in AV_3Sb_5 . These observations imply that electron-phonon coupling may play a crucial role in promoting the CDW order in ScV_6Sn_6 . Further considering the correlation effect associated with VHSs, we deduce that electron-electron interactions and electron-phonon coupling may conspire to generate the symmetry-breaking states in the vanadium-based kagome metals, which warrants further investigations, both from the theoretical and the experimental fronts.

In conclusion, our study combining ARPES and Raman scattering measurements provides important insights into the underlying mechanism of the CDW order in ScV_6Sn_6 . The VHSs located near the \bar{K}

point introduce nesting wave vectors close to $(1/3, 1/3)$, which are consistent with the observed in-plane $\sqrt{3} \times \sqrt{3}$ CDW order. Furthermore, our Raman measurements demonstrate the presence of the two-phonon mode and amplitude modes, suggesting a strong electron-phonon coupling [40]. Taken together, our results suggest a concerted mechanism of the CDW order in ScV_6Sn_6 involving both electron-phonon coupling and electron correlation effects. Further investigations are necessary to fully comprehend the interplay between these two mechanisms and their roles in promoting the unconventional CDW order in vanadium-based kagome metals.

References:

- [1] Yan, S., Huse, D. A. & White, S. R. Spin-Liquid Ground State of the $S = 1/2$ Kagome Heisenberg Antiferromagnet. *Science* **332**, 1173–1176 (2011).
- [2] Han, T.-H. *et al.* Fractionalized excitations in the spin-liquid state of a kagome-lattice antiferromagnet. *Nature* (London) **492**, 406–410 (2012).
- [3] Han, T., Chu, S. & Lee, Y. S. Refining the Spin Hamiltonian in the Spin-1/2 Kagome Lattice Antiferromagnet $\text{ZnCu}_3(\text{OH})_6\text{Cl}_2$ Using Single Crystals. *Phys. Rev. Lett.* **108**, 157202 (2012).
- [4] Ko, W. -H., Lee, P. A. & Wen, X. -G. Doped kagome system as exotic superconductor. *Phys. Rev. B* **79**, 214502 (2009).
- [5] Kiesel, M. L. & Thomale, R. Sublattice interference in the kagome Hubbard model. *Phys. Rev. B* **86**, 121105(R) (2012).
- [6] Kiesel, M. L., Platt, C. & Thomale, R. Unconventional Fermi Surface Instabilities in the Kagome Hubbard Model. *Phys. Rev. Lett.* **110**, 126405 (2013).
- [7] Wang, W.-S., Li, Z.-Z., Xiang, Y.-Y. & Wang, Q.-H. Competing electronic orders on kagome lattices at van Hove filling. *Phys. Rev. B* **87**, 115135 (2013).
- [8] Ye, L. *et al.* Massive Dirac fermions in a ferromagnetic kagome metal, *Nature* (London) **555**, 638–642 (2018).
- [9] Morali, N. *et al.* Fermi-arc diversity on surface terminations of the magnetic Weyl semimetal $\text{Co}_3\text{Sn}_2\text{S}_2$. *Science* **365**, 1286–1291 (2019).
- [10] Liu, D.-F. *et al.* Magnetic Weyl semimetal phase in a Kagomé crystal. *Science* **365**, 1282–1285 (2019).
- [11] Ortiz, B. R. *et al.* CsV_3Sb_5 : A \mathbb{Z}_2 Topological Kagome Metal with a Superconducting Ground State. *Phys. Rev. Lett.* **125**, 247002 (2020).
- [12] Jiang, Y.-X. *et al.* Discovery of unconventional chiral charge order in kagome superconductor KV_3Sb_5 . *Nat. Mater.* **20**, 1353–1357 (2021).
- [13] Zhao, H. *et al.* Cascade of correlated electron states in the kagome superconductor CsV_3Sb_5 . *Nature* **599**, 216–221 (2021).
- [14] Chen, H. *et al.* Roton pair density wave and unconventional strong-coupling superconductivity in a topological kagome metal. *Nature* **559**, 222–228 (2021).
- [15] Nie, L. *et al.* Charge-density-wave-driven electronic nematicity in a kagome superconductor. *Nature* **604**, 59–64 (2022).
- [16] Mielke III, C. *et al.* Time-reversal symmetry-breaking charge order in a correlated kagome superconductor. *Nature* **602**, 245–250 (2022).
- [17] Guguchia, Z. *et al.* Tunable unconventional kagome superconductivity in charge ordered RbV_3Sb_5 and KV_3Sb_5 . *Nat. Commun.* **14**, 153 (2023).
- [18] Tan, H., Liu, Y., Wang, Z. & Yan, B. *et al.* Charge density waves and electronic properties of superconducting kagome metals. *Phys. Rev. Lett.* **127**, 046401 (2021).

- [19] Christensen, M. H., Birol, T., Andersen, B. M. & Fernandes, R. M. Theory of the charge-density wave in AV_3Sb_5 kagome metals. *Phys. Rev. B* **104**, 214513 (2021).
- [20] Feng, X., Jiang, K., Wang, Z. & Hu, J. Chiral flux phase in the Kagome superconductor AV_3Sb_5 . *Sci. Bull.* **66**, 1384 (2021).
- [21] Denner, M. M., Thomale, R. & Neupert, T. Analysis of Charge Order in the Kagome Metal AV_3Sb_5 ($A=K, Rb, Cs$). *Phys. Rev. Lett.* **127**, 217601 (2021).
- [22] Lin, Y.-P. & Nandkishore, R. M. Complex charge density waves at Van Hove singularity on hexagonal lattices: Haldane-model phase diagram and potential realization in kagome metals AV_3Sb_5 . *Phys. Rev. B* **104**, 045122 (2021).
- [23] Park, T., Ye, M. & Balents, L. Electronic instabilities of kagomé metals: saddle points and Landau theory. *Phys. Rev. B* **104**, 035142 (2021).
- [24] Pokharel, G. *et al.* Electronic properties of the topological kagome metals YV_6Sn_6 and GdV_6Sn_6 . *Phys. Rev. B* **104**, 235139 (2021).
- [25] Peng, S. *et al.* Realizing kagome band structure in two-dimensional kagome surface states of RV_6Sn_6 ($R=Gd, Ho$). *Phys. Rev. Lett.* **127**, 266401 (2021).
- [26] Arachchige, H. W. S. *et al.* Charge density wave in kagome lattice intermetallic ScV_6Sn_6 . *Phys. Rev. Lett.* **129**, 216402 (2022).
- [27] Guguchia, Z. *et al.* Hidden magnetism in charge ordered bilayer kagome material ScV_6Sn_6 . *arXiv*:
- [28] Cheng, S. *et al.* Nanoscale visualization and spectral fingerprints of the charge order in ScV_6Sn_6 distinct from other kagome metals. *arXiv*: 2302.12227 (2023).
- [29] Hu, Y. *et al.* Tunable topological Dirac surface states and van Hove singularities in kagome metal GdV_6Sn_6 . *Sci. Adv.* **8**, add2024 (2022).
- [30] Hu, T. *et al.* Optical spectroscopy and band structure calculations of the structural phase transition in the vanadium-based kagome metal ScV_6Sn_6 . *Phys. Rev. B* **107**, 165119 (2023).
- [31] Hu, Y. *et al.* Rich nature of van Hove singularities in kagome superconductor CsV_3Sb_5 . *Nat. Commun.* **13**, 2220 (2022).
- [32] Hu, Y. *et al.* Coexistence of trihexagonal and star-of-David pattern in the charge density wave of the kagome superconductor AV_3Sb_5 . *Phys. Rev. B* **106**, L241106 (2022).
- [33] Kang, M. *et al.* Twofold van Hove singularity and origin of charge order in topological kagome superconductor CsV_3Sb_5 . *Nat. Phys.* **18**, 301–308 (2022).
- [34] Kang, M. *et al.* Charge order landscape and competition with superconductivity in kagome metals. *Nat. Mater.* **22**, 186–193 (2022).
- [35] Ohno, H., Iizuka, Y. & Fujita, S. Pure rotational Raman spectroscopy applied to N_2/O_2 analysis of air bubbles in polar firn. *J. of Glaciol.* **67**(265), 903–908 (2021).

- [36] Hill, H. M. *et al.* Phonon origin and lattice evolution in charge density wave states. *Phys. Rev. B* **99**, 174110 (2019).
- [37] Joshi, J. *et al.* Short-range charge density wave order in 2H-TaS₂. *Phys. Rev. B* **99**, 245144 (2019).
- [38] Hajiyev, P., Cong, C. & Yu, Ting. Contrast and Raman spectroscopy study of single- and few-layered charge density wave material: 2H-TaSe₂. *Sci. Rep.* **3**, 2593 (2013).
- [39] Liu, G. *et al.* Observation of anomalous amplitude modes in the kagome metal CsV₃Sb₅. *Nat. Commun.* **13**, 3461 (2022).
- [40] Klein, M. V. Theory of two-phonon Raman scattering in transition metals and compounds. *Phys. Rev. B* **24**, 4208 (1981).
- [41] Sooryakumar, R. & Klein, M. V. Effect of nonmagnetic impurities on the Raman spectra of the superconductor niobium diselenide. *Phys. Rev. B* **23**, 3222 (1981).
- [42] Moncton, D. E. Axe, J. D. & DiSalvo, F. J. Study of Superlattice Formation in 2H-NbSe₂ and 2H-TaSe₂ by Neutron Scattering. *Phys. Rev. Lett.* **34**, 734 (1975).
- [43] Tan, H. & Yan, B. Abundant lattice instability in kagome metal ScV₆Sn₆. *arXiv*: 2302.07922 (2023).
- [44] Grüner, G. Density Waves in Solids. Advanced book program: Addison-Wesley (Perseus Books Group, 2000).
- [45] Wen, J., Rüegg, A., Joseph Wang, C.-C. & Fiete, Gregory A. Interaction-driven topological insulators on the kagome and the decorated honeycomb lattices. *Phys. Rev. B* **82**, 075125 (2010).
- [46] Tan, H., Liu, Y., Wang, Z. & Yan, B. Charge density waves and electronic properties of superconducting kagome metals. *Phys. Rev. Lett.* **127**, 046401 (2021).
- [47] Ortiz, B. R. *et al.* Fermi surface mapping and the nature of charge-density-wave order in the kagome superconductor CsV₃Sb₅. *Phys. Rev. X* **11**, 041030 (2021).
- [48] Kuzmenko, A. B. Kramers–Kronig constrained variational analysis of optical spectra. *Rev. Sci. Instrum.* **76**, 083108 (2005).
- [49] Kresse, G. & Hafner, J. Ab initio molecular dynamics for liquid metals. *Phys. Rev. B* **47**, 558–561 (1993).
- [50] Kresse, G. & Furthmüller, J. Efficiency of ab-initio total energy calculations for metals and semiconductors using a plane-wave basis set. *Comput. Mater. Sci.* **6**, 15–50 (1996).
- [51] Kresse, G. & Furthmüller, J. Efficient iterative schemes for *ab initio* total-energy calculations using a plane-wave basis set. *Phys. Rev. B* **54**, 11169–11186 (1996).
- [52] Perdew, J. P. Burke, K. & Ernzerhof, M. Generalized gradient approximation made simple. *Phys. Rev. Lett.* **77**, 3865–3868 (1996).
- [53] Mostofi, A. A. *et al.* An updated version of wannier90: A tool for obtaining maximally-localised Wannier functions. *Comput. Phys. Commun.* **185**, 2309–2310 (2014).

[54] Lopez Sancho, M. P., Lopez Sancho, J. M., Sancho, J. M. L. & Rubio, J. Highly convergent schemes for the calculation of bulk and surface Green functions. *J. Phys. F* **15**, 851–858 (1985).

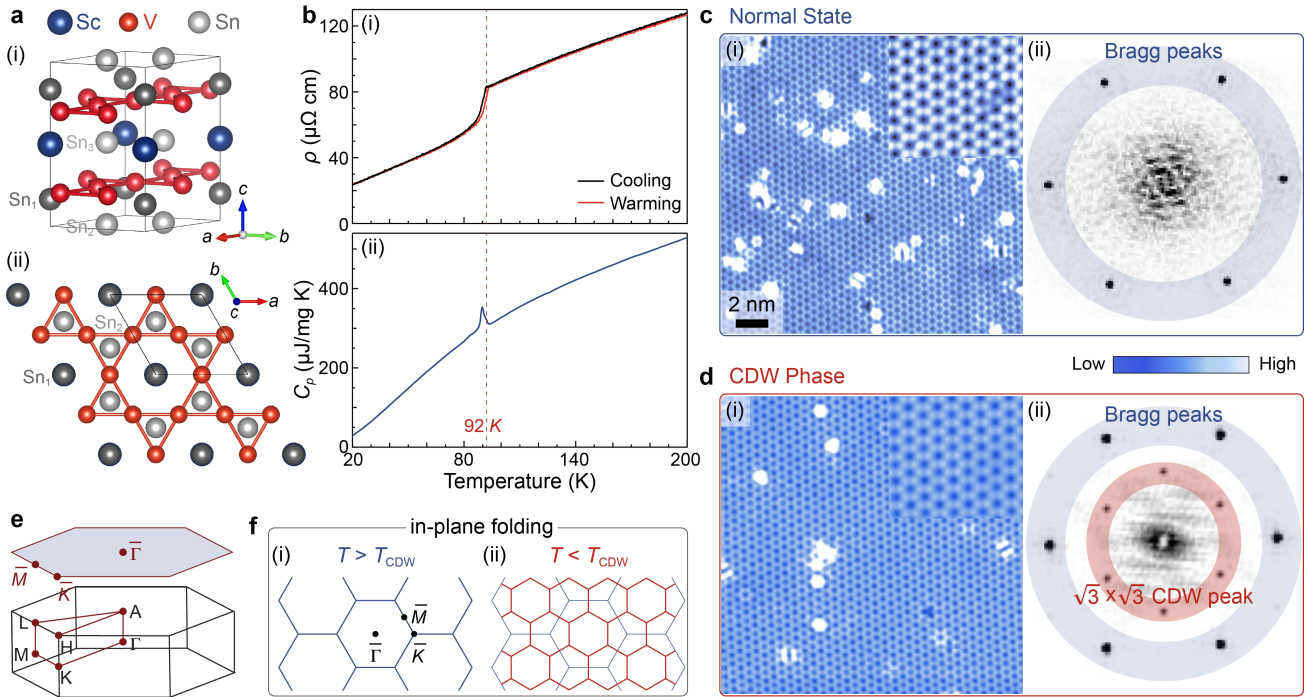


Fig. 1. Crystal structure, transport and topographic characterizations of ScV_6Sn_6 . **a** Crystal structure in the normal state showing the unit cell (i) and top view displaying the kagome lattice (ii). **b** Temperature-dependent ab -plane resistivity (i) and specific heat capacity (ii) of ScV_6Sn_6 , indicating the onset of CDW near 92 K. **c** STM topograph of Sn^2 termination measured at 80 K (i) and associated Fourier transforms (ii). Atomic Bragg peaks are highlighted with a blue ring. **d** Same as I, but taken at 1 K. $\sqrt{3} \times \sqrt{3}$ $R30^\circ$ CDW peaks are marked with a red ring. **e** Schematic of the bulk and surface Brillouin zones (BZs), with high-symmetry points marked. **f** Schematics of the in-plane folding of the surface BZ. Pristine (i) and CDW (ii) BZs are shown with blue and red lines, respectively.

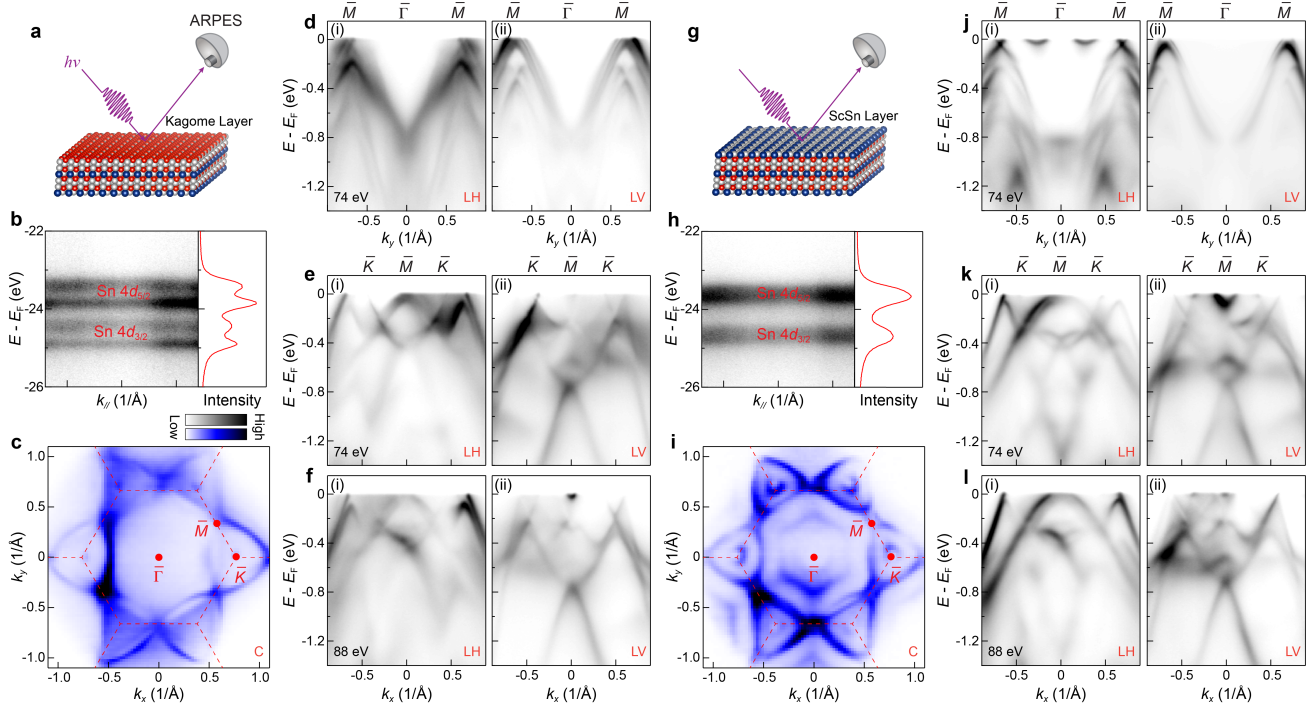


Fig. 2. Termination-dependent photoemission measurements of the electronic structure in ScV_6Sn_6 . **a** Schematic of the kagome termination. **b** The corresponding x-ray photoelectron spectroscopy (XPS) spectrum on the Sn 4d core levels (left) and the integrated energy distribution curve (EDC) of the core levels (right). **c** Fermi surface (FS) mapping collected on the kagome termination, measured with circular (C) polarized light. The dashed red line represents the pristine BZ. **d** Photoelectron intensity plots of the band structure taken along the $\bar{\Gamma} - \bar{M}$ direction on the kagome termination, measured with 74 eV linear horizontal (LH) (i) and linear vertical (LV) (ii) polarizations. **e,f** Same as (d), but taken along the $\bar{\Gamma} - \bar{K}$ direction, measured with 74 eV (e) and 88 eV (f). **g-l** Same as (a-f), but measured on the ScSn^{32} termination.

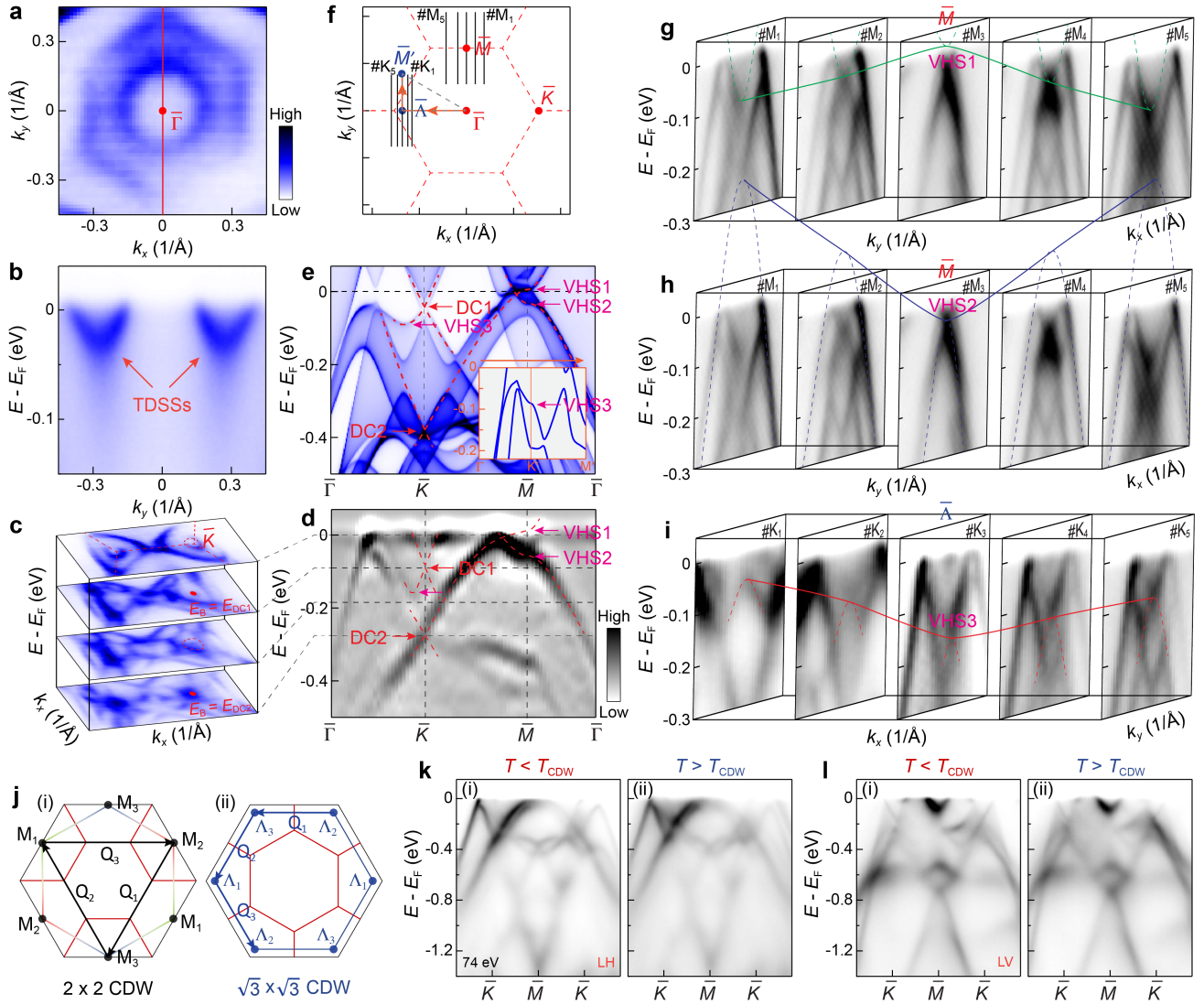


Fig. 3. \mathbb{Z}_2 topological surfaces states, Dirac cones and VHSs in ScV_6Sn_6 . **a** Zoom-in FS mapping measured on the Sn termination. **b** ARPES spectrum taken along the $\bar{\Gamma} - \bar{M}$ direction highlighting the TDSSs. The momentum path is indicated by the red line in (a). **c** Stacking plots of constant energy maps around the \bar{K} point. **d** Energy-momentum dispersion along the $\bar{\Gamma} - \bar{K} - \bar{M} - \bar{\Gamma}$ direction. **e** Calculated band structure along the $\bar{\Gamma} - \bar{K} - \bar{M} - \bar{\Gamma}$ direction. Dirac cone (DC) and VHS are indicated by red and pink arrows, respectively. The inset displays DFT bands along the $\bar{\Gamma} - \bar{\Lambda} - M'$ direction [as indicated by the orange arrow in (f)]. **f** Schematics of the surface BZ. **g** A series of cuts taken vertically across the $\bar{K} - \bar{M}$ path, the momentum paths of the cuts ($\#M_1$ - $\#M_5$) are indicated by the black lines in (f). Dashed green curve highlights the electron-like band and solid curve indicates the corresponding VHS1 at the \bar{M} point. **h** Same as (g), but highlights the hole-like band (dashed blue curve) and VHS2 (solid curve). **i** Stack of cuts perpendicular to the $\bar{\Gamma} - \bar{K}$ direction. The momentum directions of the cuts ($\#K_1$ - $\#K_5$) are indicated by the black lines in (f). Dashed red curve and solid curve indicate the hole-like band and corresponding VHS3 at the $\bar{\Lambda}$ point, respectively. The ARPES spectra shown in (g-i) were taken with 74 eV C polarized light. **j** FS of kagome lattice at the VHS filling. The three inequivalent saddle points M_i (Λ_i) are connected by three inequivalent nesting vectors Q_i , which can give rise to a 2×2 CDW (i) and $\sqrt{3} \times \sqrt{3}$ CDW (ii). **k** Temperature-dependent measurements of the band structure along the $\bar{\Gamma} - \bar{K}$ direction, measured below T_{CDW} at 20 K (i) and above T_{CDW} at 130 K (ii) with 74 eV LH polarized light. **l** Same as (b), but measured with LV polarization.

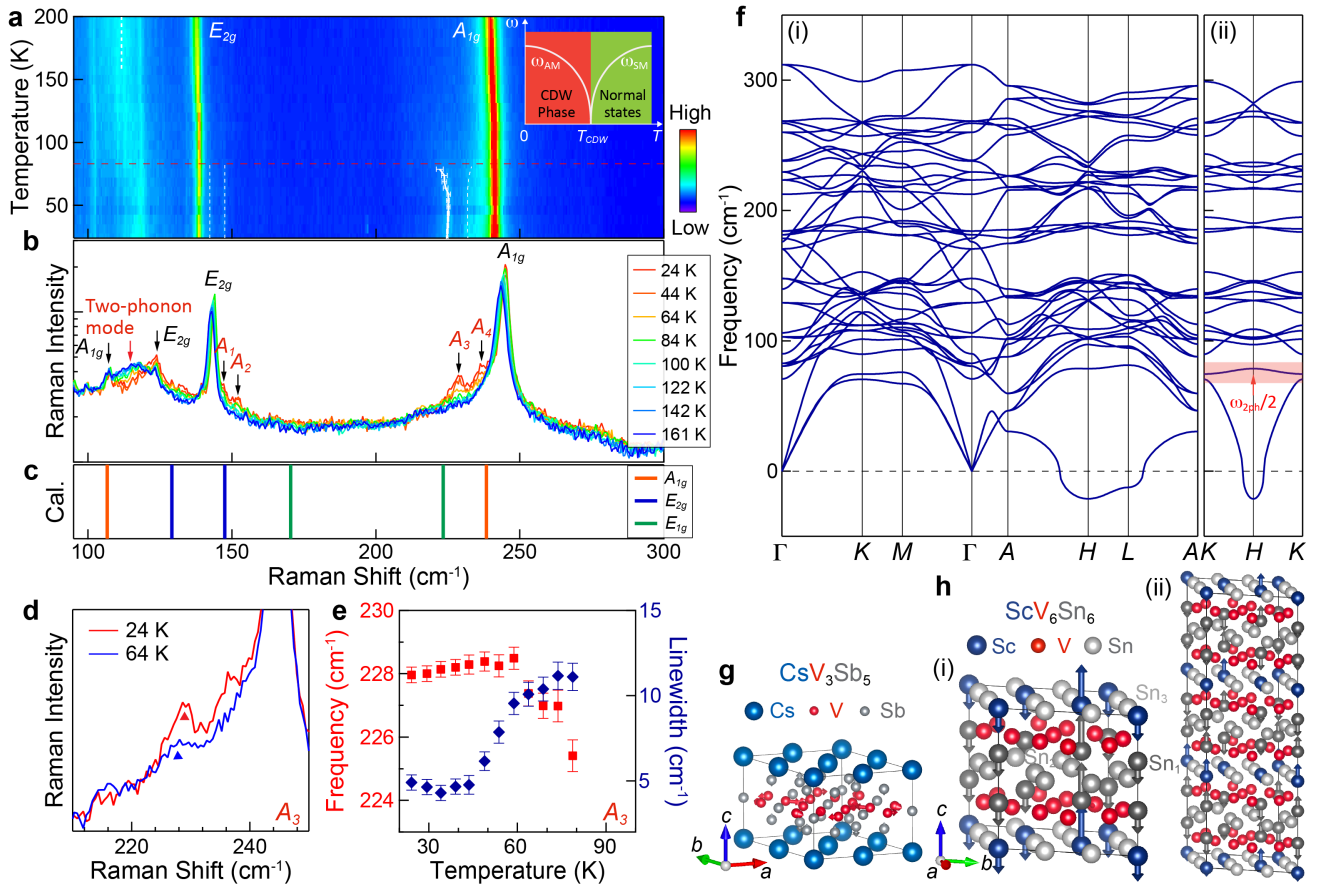


Fig. 4. Raman modes and phonon band structure in ScV_6Sn_6 . **a** Temperature-dependent colormap of the Raman response recorded on ScV_6Sn_6 . The inset illustrates the relationship between the soft mode and amplitude mode in typical CDW materials. The soft mode frequency (ω_{SM}) freezes below T_{CDW} , and the amplitude mode frequency (ω_{AM}) emerges afterward. **b** Typical Raman spectra measured below and above T_{CDW} . **c** Calculated Raman mode frequencies around Γ point. **d** Raman spectra measured at 24 K and 64 K. The triangle indicates the A_3 phonon peak. **e** Temperature dependence of the Frequency and linewidth of the A_3 mode. **f** DFT calculated phonon band structure along high-symmetry paths (i) and the $K - H - K$ path (ii) of pristine ScV_6Sn_6 , with experimental lattice parameters [26]. The red shaded region indicates the half frequency of the two-phonon mode. **g** Distortion pattern of the trihexagonal pattern in the $2 \times 2 \times 1$ CDW phase of CsV_3Sb_5 . **h** Acoustic phonon mode at the K point (i) corresponding to the observed two-phonon mode in (a, b) and distortion pattern (ii) of the $\sqrt{3} \times \sqrt{3} \times 3$ CDW indicated by the vectors, with respect to the pristine phase of ScV_6Sn_6 [Fig. 1a(i)]. The length of the vectors represents the amplitude of atomic displacements.